ARTICLES
https://doi.org/10.1038/s41561-022-00899-1

nature geoscience

Decline in bulk deposition of air pollutants in China lags behind reductions in emissions

Yu Zhao[1]✉, Mengxiao Xi[1,2], Qiang Zhang[3], Zhaoxin Dong[4], Mingrui Ma[1], Kaiyue Zhou[1], Wen Xu[5], Jia Xing[4], Bo Zheng[6], Zhang Wen[5], Xuejun Liu[5], Chris P. Nielsen[7], Yang Liu[8], Yuepeng Pan[9] and Lei Zhang[1]

Swift changes in both industrialization and pollution control in China over the past 15 years have created a complex and evolving relationship between emission sources and the depositional sinks of air pollutants. Here, by combining an emissions inventory, an air quality model and a statistical model to estimate bulk deposition (wet plus a part of dry), we present the changes and driving factors of source–sink relationships of typical pollutants throughout China between 2005 and 2020. We find that the deposition of sulfate and nitrate has declined more slowly than the emissions of their precursors, sulfur dioxide and nitrogen oxides, which we attribute, in part, to increased precipitation. In four developed regions of China, enhanced air pollution transport also plays an important role in the slower decline of deposition compared with that of emissions, as has a changing aerosol chemistry in the case of sulfur compounds. Our analysis shows that reducing deposition is not as simple as merely reducing its precursor emissions and suggests that the design of future policies to reduce associated risks may need to vary by region and species, accounting for their evolving interactions over time.

China is a leading national source of air pollutant emissions, which include sulfur dioxide (SO_2), nitrogen oxides (NO_x) and ammonia (NH_3) (refs. [1,2]), and therefore suffers high deposition (or sinks) of air pollutants that damage biological diversity and ecological health[3–6]. For the past 15 years, air pollution control in China has resulted in different rates of reduction in emissions of various species that differ also by region, as indicated by recent emissions inventory studies, for example, the Multiple-resolution Emission Inventory for China (MEIC, http://www.meicmodel.org). Measured from space, the vertical column densities (VCDs) of SO_2 and NO_2 have also declined across the country[7,8]. However, the relationships between emissions and deposition, which connect anthropogenic activities to ecosystem risks and usually vary by region and time[5,9,10], are rarely evaluated. With limited ground observations of deposition, there are insufficient high-resolution data to match those currently available for emissions. The spatiotemporal evolution of source–sink relationships of air pollutants remains poorly understood, and how they are driven by pollution controls and the meteorological factors that influence the formation and scavenging of atmospheric species have not been rigorously quantified. Such research gaps prevent a full understanding of the benefits of emissions control on deposition and undermine effective policy-making to reduce ecosystem risks.

Here, we developed a generalized additive model (GAM) by integrating multiple datasets to estimate the nationwide sulfate (SO_4^{2-}), nitrate (NO_3^-) and ammonium (NH_4^+) bulk deposition from 2005 to 2020. The model relies on the best available observational data on deposition, with a sufficient accuracy and representativeness in terms of geophysical location and land use type (Methods). The ratios of bulk deposition to emissions (D/E) were applied to illustrate the source–sink relationships of the three species. The driving factors of the changing relationship are identified with GAM and an air quality response surface model (RSM). We found that, in addition to precipitation, the changing regional pollution transport is an important determinant for the rising D/E ratios for sulfate and nitrate in four developed regions in recent years, and changes in aerosol chemistry were another factor in the case of sulfate. Our analysis highlights the impact of differing rates of emission control of regions and species on changing source–sink relationships, and informs better strategies to protect against ecosystem risk.

Spatial and temporal patterns of bulk deposition in China

The average bulk deposition (wet plus a part of dry) of SO_4^{2-}, NO_3^- and NH_4^+ in China was estimated at 9.6 ± 0.7, 4.8 ± 0.2 and $6.5 \pm 0.4\,kg_{S/N})\,ha^{-1}\,yr^{-1}$, respectively, during 2005–2020 for SO_4^{2-} and NO_3^- and 2008–2020 for NH_4^+. Four economically developed key regions (Jing-Jin-Ji (JJJ), Yangtze River Delta (YRD), Pearl River Delta (PRD) and Sichuan Basin (SCB); see the locations in Supplementary Fig. 1) account collectively for 27, 24 and 26% of the national deposition of SO_4^{2-}, NO_3^- and NH_4^+, respectively (Extended Data Fig. 1 and Extended Data Table 1). Compared with the deposition, emissions of the source gases are more concentrated in the four regions, with their collective fractions reaching 38, 41 and 34% for SO_2, NO_x and NH_3, respectively (Supplementary Fig. 2

[1]State Key Laboratory of Pollution Control & Resource Reuse and School of Environment, Nanjing University, Nanjing, China. [2]Environmental Big Data Science Center, Research Institute for Environmental Innovation Suzhou Tsinghua, Suzhou, China. [3]Ministry of Education Key Laboratory for Earth System Modeling, Department for Earth System Science, Tsinghua University, Beijing, China. [4]School of Environment, and State Key Joint Laboratory of Environment Simulation and Pollution Control, Tsinghua University, Beijing, China. [5]College of Resources and Environmental Sciences, China Agricultural University, Beijing, China. [6]Institute of Environment and Ecology, Tsinghua Shenzhen International Graduate School, Tsinghua University, Shenzhen, China. [7]Harvard-China Project on Energy, Economy and Environment, John A. Paulson School of Engineering and Applied Sciences, Harvard University, Cambridge, MA, USA. [8]Gangarosa Department of Environmental Health, Rollins School of Public Health, Emory University, Atlanta, GA, USA. [9]State Key Laboratory of Atmospheric Boundary Layer Physics and Atmospheric Chemistry (LAPC), Institute of Atmospheric Physics, Chinese Academy of Sciences, Beijing, China. ✉e-mail: yuzhao@nju.edu.cn

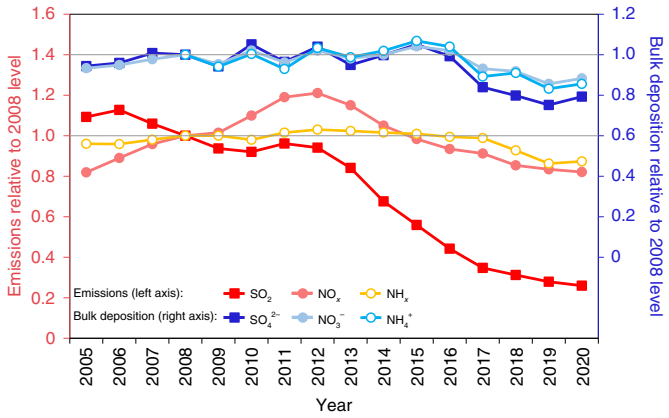

Fig. 1 | The interannual variations of emissions (left axis) and deposition (right axis) for China. All the data are relative to the 2008 levels. The grey horizontal lines are a visual guidance for 1.0 on each of the *y* axes.

and Extended Data Table 1). Clear differences exist in the seasonal patterns of emissions and deposition. Larger SO_2 and NO_x emissions occur in the winter due to the enhanced coal burning for heating, whereas larger NH_3 emissions in the summer result from elevated fertilizer volatilization (Supplementary Fig. 3a). The highest deposition occurs in the summer for all species, associated with a high precipitation (Supplementary Fig. 3b).

Figure 1 compares the interannual changes in the national bulk deposition estimated here with the emissions from MEIC (see the regional results in Supplementary Fig. 4). Owing to the continuously expanded use of flue gas sulfurization (FGD) in power and industrial sectors, the annual SO_2 emissions are estimated to have declined by 76% from 2005 to 2020. The control of NO_x was limited until 2012, which allowed annual emissions to grow 49% from 2005 to 2012. Since 2013, selective catalytic reduction (SCR) has been applied in power and cement sectors, which resulted in a 32% reduction in NO_x annual emissions from 2012 to 2020. The interannual variation in NH_3 emissions is smaller. Compared with the emissions, smaller and more irregular changes exist in the bulk deposition. The largest reduction is found for SO_4^{2-} after 2012, attributed mainly to the improved SO_2 controls compared with those of earlier years.

As summarized in Table 1, the annual changes of SO_4^{2-} deposition from 2005 to 2012 for the four key regions (JJJ, YRD, SCB and PRD) and the whole country were calculated as 0.34, 0.29, −0.27, −0.17 and 0.07 $kg_S\,ha^{-1}\,yr^{-1}$ respectively, followed by larger reductions from 2012 to 2020 at −1.15, −1.14, −1.01, −0.92 and −0.35 $kg_S\,ha^{-1}\,yr^{-1}$. A slight growth in NO_3^- deposition was found up to 2012, followed by reductions of −0.26, −0.32, −0.19, −0.20 and −0.10 $kg_N\,ha^{-1}\,yr^{-1}$ during 2012–2020 for the four regions and the whole country, respectively. Attributable to the earlier and broader use of FGD, a greater abatement of SO_2 was achieved than that of NO_x over the past decade, which led to the faster reduction in SO_4^{2-} deposition compared with that for NO_3^-. The declines in deposition are slower than those of emissions or VCDs. Although the SO_2 and NO_x emissions declined, respectively, by 16.9 and 4.4% yr^{-1} nationwide during 2012–2020, the corresponding declines in VCDs were 4.4 and 4.2% yr^{-1}, and those of deposition were even less, at 4.0 and 2.1% yr^{-1}, respectively. The results imply a limited benefit of emission control on deposition.

The mean absolute deviations (an indicator of the temporal heterogeneity of a spatial distribution of concern) of deposition are larger than those of emissions for all the three species, which suggests a more heterogeneous evolution of the spatiotemporal patterns of deposition (Supplementary Fig. 5). The largest correlation coefficients (R) were found between deposition and precipitation, which implies a strong influence of precipitation on the changing deposition. Precipitation is identified as the most important term in GAM, as it accounts for 31, 48 and 31% of the bulk deposition variability for SO_4^{2-}, NO_3^- and NH_4^+, respectively, followed by satellite-derived VCDs (Supplementary Table 1).

The changing source–sink relationship (*D*/*E*) of pollutants

Figure 2 shows the spatial patterns of D/E ratios during 2005–2020. The D/E ratios to the east of the 'Hu-line' (a widely used southwest-to-northeast geographical division of China, which separates regions of differing climates and population densities) are generally smaller than those to the west. For example, the relatively low D/E ratios for the four key regions identify them as major sources of air pollutants, and likely to influence the air pollution levels in surrounding regions. Associated with different human activities, moreover, the D/E ratios for sulfur and oxidized nitrogen (OXN) are smaller in urban regions than those in rural ones, whereas that for reduced nitrogen (RDN) is slightly larger in urban areas (Supplementary Table 2). Transportation and industries result in larger NO_x and SO_2 emissions in urban locales, and extensive agricultural activities enhance NH_3 in rural ones. The highest D/E ratios occur in the summer for all species (Supplementary Fig. 3c), and the weakest seasonal variation is found for RDN (indicated by the smallest coefficient of variation). The higher emissions in winter but larger deposition in summer for sulfur and OXN lead to more varied D/E ratios between seasons. Moreover, stronger seasonal variations exist in northern China (JJJ, Supplementary Fig. 3d) than in southern China (YRD and PRD, Supplementary Fig. 3e,f). As central heating is mainly concentrated in the north, the elevated SO_2 and NO_x emissions from coal burning reduce the D/E ratios in winter and enlarge the seasonal variation.

Figure 3a–c compares the temporal variations of D/E ratios from 2005 to 2020 for East and West China (see the area definition in Supplementary Fig. 1), and Fig. 3d–f for the four key regions within East China. The D/E ratio for sulfur has grown almost continuously in East China (Figs. 2 and 3a), as with the four developed regions (Fig. 3d). For the West China, the D/E ratio declined until 2012 and then started to grow. The D/E ratios of OXN for most regions declined in the earlier years and increased more recently. More specifically, the turning point for West China was around two years later than that for East China, which probably results from a later implementation of emissions control policies (Fig. 3b). These temporal patterns are consistent with the differences in the progress of emission controls regionally in China. Most emission control measures were first implemented in the highly developed regions of East China and then applied more widely afterwards (Supplementary Table 3). The lack of comparable control policies for NH_3 probably explains the absence of any clear interannual trend in the D/E ratio for RDN (Fig. 3c,f).

To evaluate the impact of uncertainty from the emission estimations, we compared MEIC with other emission inventories based on 'bottom-up' methods, as well as the estimates constrained by satellite observations (the so-called 'top-down' methods (Methods)). The differences in annual emissions of all other estimates relative to MEIC range were −40 to +42%, −44 to +12% and −14 to +43% for SO_2, NO_x and NH_3, respectively (Supplementary Fig. 6a–c). Those differences resulted in changed D/E ratios but similar interannual variabilities (Supplementary Fig. 6d–f). For sulfur and OXN, smaller coefficient of variations of the D/E ratios induced by different emission datasets were generally found for recent years (Supplementary Fig. 7), which implies a more robust estimation of the source–sink relationships.

The response of dry and wet deposition to emissions can be quite different[11], but they cannot be separated out from bulk deposition due to a lack of direct measurements of dry deposition in China.

Table 1 | Average annual changes in bulk deposition, emissions and VCDs of sulfur and OXN by region for 2005–2020

Region	Annual change ($kg_{S/N}\ ha^{-1}\ yr^{-1}$ for deposition and emissions; $10^{15}\ mol\ cm^{-2}\ yr^{-1}$ for VCDs)											
	Sulfur						OXN					
	Deposition		Emissions		VCDs		Deposition		Emissions		VCDs	
	P1	P2	P1	P2	P1	P2	P1	P2	P1	P2	P1	P2
JJJ	0.34	−1.15	−3.60	−7.16	−0.54	−3.35	0.10	−0.26	2.93	−2.55	0.99	−0.97
YRD	0.29	−1.14	−2.57	−3.41	−0.13	−1.35	0.10	−0.32	2.02	−1.79	0.50	−0.42
SCB	−0.27	−1.01	−1.78	−5.37	−0.43	−0.93	0.01	−0.19	1.11	−0.68	0.14	0.05
PRD	−0.17	−0.92	−0.05	−2.27	−0.38	0.04	0.02	−0.20	0.48	−0.97	−0.08	0.12
China	0.07	−0.35	−0.39	−1.35	−0.05	−0.23	0.04	−0.10	0.60	−0.46	0.16	−0.05
Relative annual change rate (% yr^{-1})	P1	P2	P1	P2	P1	P2	P1	P2	P1	P2	P1	P2
JJJ	1.92	−7.89	−4.51	−18.60	−2.10	−14.67	1.16	−3.38	4.89	−4.56	7.27	−8.24
YRD	1.10	−4.61	−5.91	−18.13	−0.96	−6.94	0.90	−3.07	4.36	−4.11	5.75	−4.86
SCB	−1.14	−5.42	−3.29	−21.38	−2.91	−10.25	0.06	−2.28	6.01	−3.54	4.99	4.47
PRD	−0.79	−5.51	−0.19	−15.94	−3.59	0.58	0.23	−3.13	1.64	−3.88	−1.75	1.89
China	0.93	−3.99	−2.58	−16.92	−0.06	−4.39	0.91	−2.08	5.47	−4.43	1.62	−4.24

The annual change was estimated as the slope of the least-squares regression between the *D/E* ratios/satellite-derived VCD and the number of years, and the relative annual change rate is the ratio of the annual change to the average *D/E* ratios/satellite-derived VCD during the research period. P1, 2005–2012; P2, 2012–2020. OXN, oxidized nitrogen.

To explore the differences, we calculated the *D*/*E* ratios for the dry deposition of OXN, RDN and SO_2 based on two datasets of dry deposition from 2011 to 2018, estimated with the 'inferential method'[12,13] (Methods). The interannual variations of OXN and SO_2 are estimated at −2.3 and 2.5% yr^{-1}, respectively (Supplementary Fig. 8), both smaller than those for bulk deposition (4.5% and 24.3% yr^{-1}). The comparison indicates that dry deposition is more influenced by nearby sources and responds more directly to emissions. The hotspots of NO_2 dry deposition in the developed eastern China indicate the impact of intensive industry and transportation activities, whereas those of SO_2 in northern China indicate the effect of coal burning[13] (Supplementary Fig. 9). For RDN, however, a larger interannual variability of the *D*/*E* ratio was found for dry deposition (2.7% yr^{-1}) than for bulk deposition (0.1% yr^{-1}). The sharply reduced SO_2 emissions are believed to elevate the gaseous NH_3 level in the atmosphere and thereby the *D*/*E* ratio[14].

The main driving factors of changing *D/E* ratios

We explored the driving factors for the varied *D*/*E* ratios for sulfur and OXN. Precipitation, identified as the most important term in GAM, increased at a rate of 6.3 mm yr^{-1} for China during 2005–2020. We recalculated the bulk deposition and *D*/*E* ratios excluding the variation of precipitation and that of all the meteorological factors in GAM. The annual average bulk deposition without a change in precipitation was smaller than that with it for both sulfate (2005–2020) and nitrate (2012–2020) for the whole country and the four key regions (Supplementary Fig. 10). Accordingly, the annual average *D*/*E* ratios for sulfur and OXN would decline by 6 and 3% for the entire country and 6–15% and 5–14% for the four key regions, respectively (Supplementary Table 4). Slight differences in both deposition and *D*/*E* ratios were found when all the meteorological terms were fixed (Supplementary Fig. 10 and Supplementary Table 4). Therefore, the increased precipitation probably offsets part of the benefit of emissions control on the deposition and increase in *D*/*E* ratios.

Other factors that influence *D*/*E* ratio include changes in the regional pollution transport and the chemistry of aerosol formation, attributed, in part, to the varied progress of emission controls by region and, in part, to the substantial emission reduction of certain species, such as SO_2 (refs. [15,16]), respectively. We applied an air quality RSM[17] to simulate the response of sulfate–nitrate–ammonium (SNA) aerosol concentrations to the interannual changes in emissions, and used the conversion rate of precursor emissions to SNA (SNA/*E*) as a surrogate for the response of deposition to emissions for the four key regions. The application can be justified by the strong correlations between the simulated SNA concentration and deposition (Supplementary Fig. 11). Besides the base simulation (Base), three hypothetical scenarios were developed to quantify the contribution of local emissions to SNA (No-Local-Emis), the impacts of changed aerosol chemistry (No-Species-Chg) and the impacts of regional transport (No-Region-Diff) on SNA production during 2005–2020 (see the details in Methods).

Indicated by the difference between Base and No-Local-Emis, the shares of sulfate concentrations attributable to local emissions declined by 8–25 percentage points for the four key regions, and the analogous numbers for nitrate are smaller, ranging from 3 to 8 percentage points (Supplementary Fig. 12). The reduced local contribution to SNA implies an increased role for the regional transport of pollution, as the most stringent emissions controls were preferentially enacted in developed and polluted regions compared with those in the surrounding areas.

Figure 4 illustrates the relative differences (RDs) of SNA/*E* between Base and No-Species-Chg or No-Region-Diff (see an example of sulfate simulation for the three scenarios in Supplementary Fig. 13). For sulfate (Fig. 4a–d), the differences between Base and No-Species-Chg increased after 2012 with positive values in most cases, which indicates the enhanced formation of sulfate aerosols, probably attributable to the reduced emissions of NO_x and increased emissions of volatile organic compounds (VOCs)[18]. Under a VOC-limited regime of ozone formation in developed regions[19], the growth of VOCs and abatement of NO_x in recent years have raised the ozone level and resulted in a lower removal of hydroxyl radicals, the key reactive species for homogeneous or aqueous-phase paths of sulfate production[17]. With abundant NO_x, moreover, a negative sensitivity to NO_x was found for sulfate[20], as the reduced

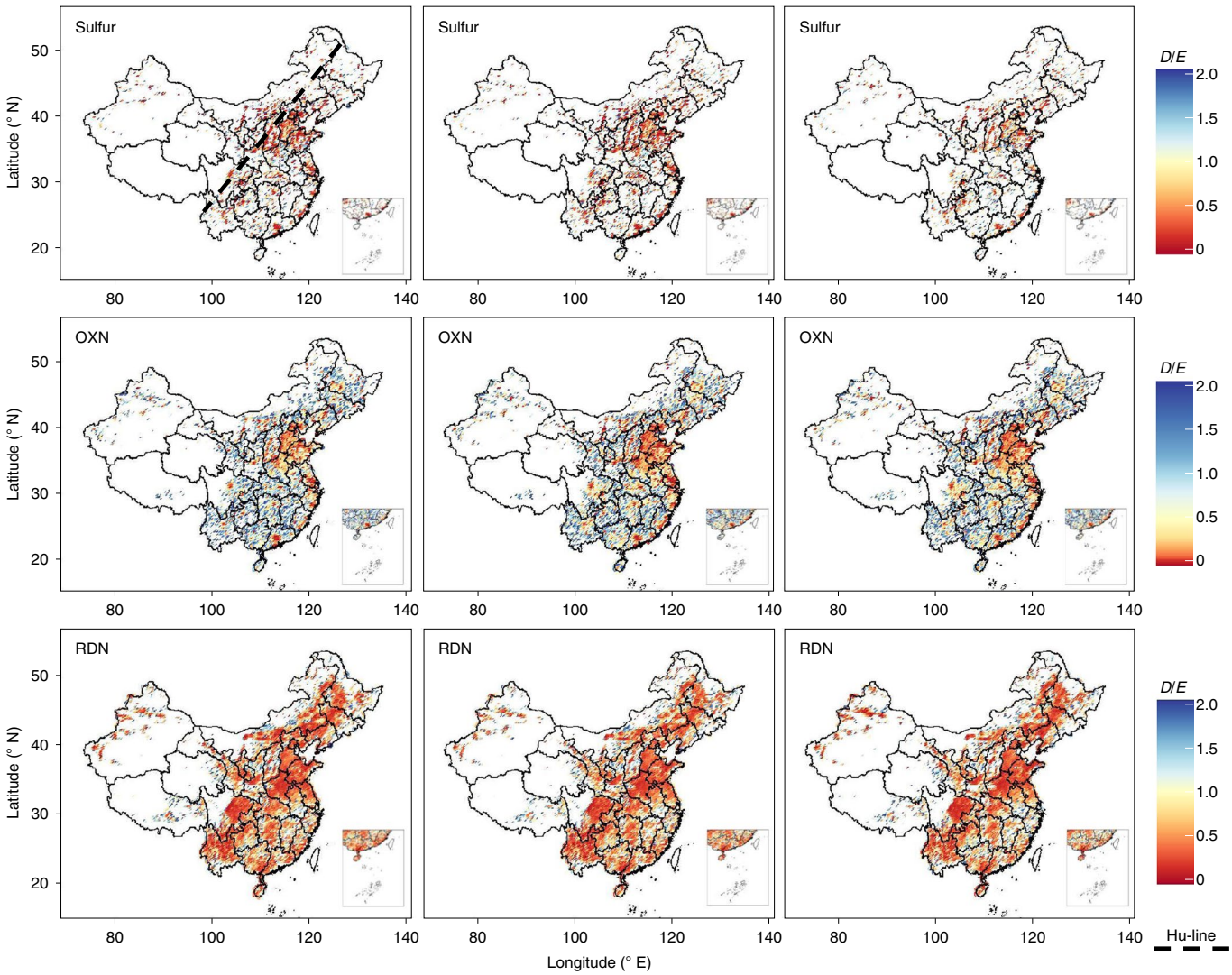

Fig. 2 | The spatial patterns of average *D/E* ratios of sulfur, OXN and RDN over China. The left, central and right columns indicate the average for 2005–2009 (2008–2009 for RDN), 2010–2014 and 2015–2020, respectively. The horizontal resolution is 0.25° latitude × 0.25° latitude. The Hu-line is shown in the first panel in the top-left corner.

NO_x accelerates the reaction between SO_2 and NH_3. For nitrate (Fig. 4e–h), the differences between Base and No-Species-Chg generally decreased during 2005–2020 and the values were negative after 2013, which indicates the suppressed formation of nitrate aerosols. Under NH_3-rich conditions with low levels of SO_2, the reduced SO_2 emissions and thereby reduced SO_4^{2-} and NH_4^+ could elevate the equilibrium constant of NH_4NO_3, and weaken the transformation of nitrate from liquid into a particulate phase, as a result of the thermodynamic effect[20].

The differences between Base and No-Region-Diff increased, except for those for sulfate in PRD and nitrate in SCB, and the values were positive after 2010 for both species. The usually smaller SNA/*E* in No-Region-Diff compared that in Base suggests that, in recent years, the regional transport played an increasingly important role on the relationship between the ambient aerosol levels and local emissions. Table 2 summarizes the relative contributions of the aerosol formation chemistry and regional transport to the changed SNA/*E* based on the disparities between Base and No-Species-Chg or No-Region-Diff shown in Fig. 4. For the four key regions, the contributions from regional transport ranged from 51 to 88% for sulfate, larger than those for nitrate (19–77%). This results partly from the more important role of local emissions to nitrate than sulfate (Supplementary Fig. 12). Along with the clearly reduced contributions of local emissions to sulfate in YRD and to nitrate in PRD (Supplementary Fig. 12), regional transport was found to play an increasingly important role on the varied SNA/*E* values for the corresponding species in those regions. Increased contributions of the changed aerosol chemistry were found for both species in JJJ, partly attributable to the swift changes in air pollutant emissions in recent years in the region.

Combining the analyses using GAM and RSM to summarize, the enhanced *D*/*E* ratios of sulfur for the developed regions in China can be attributed mainly to the increased precipitation, strengthened regional transport and changed aerosol formation, whereas that for OXN can be mainly attributed to the first two causes. Besides meteorology factors, the results reveal that the disparities of China's emissions control for different regions and species weakened its benefit on atmospheric deposition, particularly for regions with a developed industrial economy and high population density.

Policy implication and uncertainty

We demonstrate the changing source–sink relationships of air pollutants associated with the spatiotemporal disparities in emissions control in China. The slower decline in bulk deposition than that

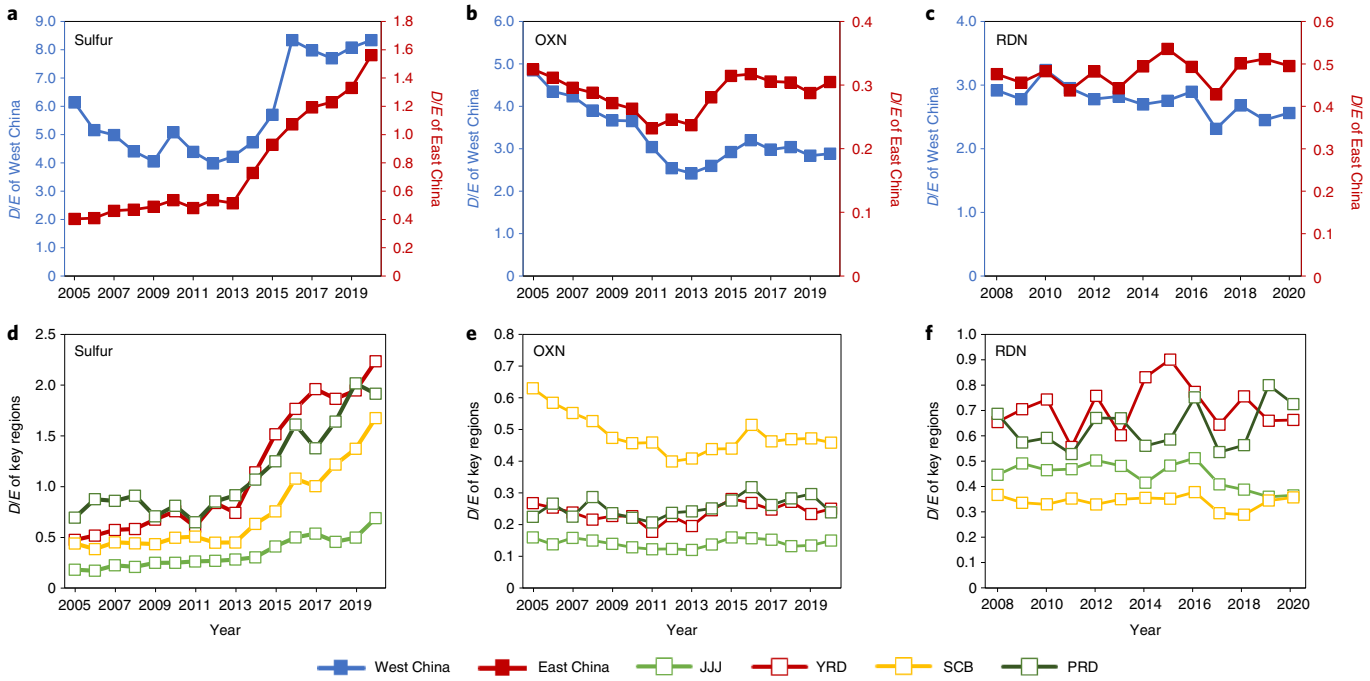

Fig. 3 | The interannual variations of the average *D/E* ratios of sulfur, OXN and RDN by region. a–c, The values for East and West China. **d–f**, The values for the four key regions: JJJ, YRD, SCB and PRD.

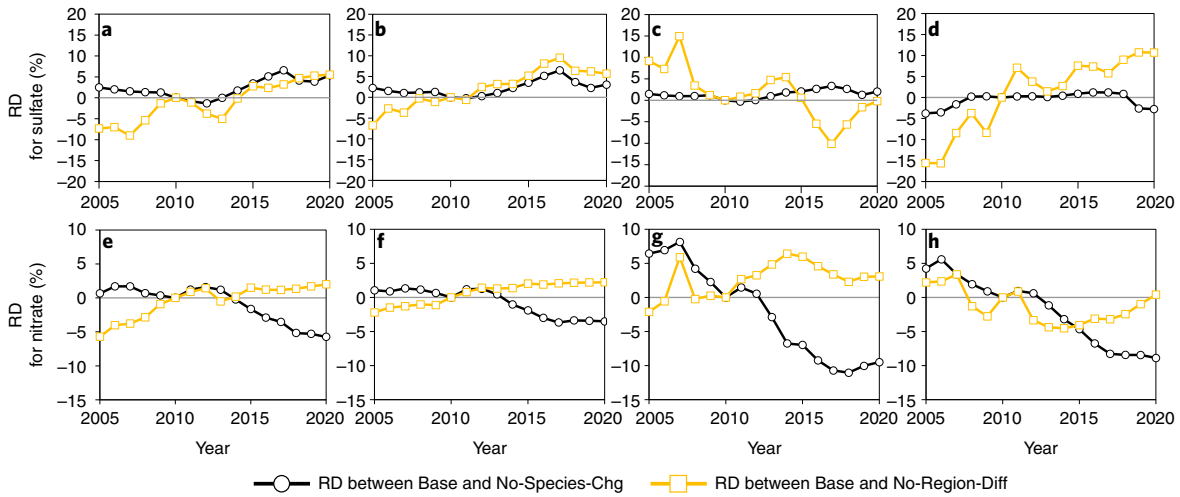

Fig. 4 | The RDs of SNA/*E* between Base and No-Species-Chg or No-Region-Diff scenarios. a–d, Sulfate for JJJ (**a**), YRD (**b**), SCB (**c**) and PRD (**d**). **e–h**, Nitrate for JJJ (**e**), YRD (**f**), SCB (**g**) and PRD (**h**). The grey horizontal line is a visual guidance for 0 on the *y* axis.

of emissions implies a persistent challenge in reducing its ecological risks. Taking ecosystem acidification as an example, atmospheric deposition was expected to prevent an apparent decline in the base cation that leached from watershed soils and in the base cation concentrations of water bodies[21]. It is thus necessary to rethink the recovery progress from acidification based on the long-term source–sink relationships of air pollutants, and a more careful strategy in emissions abatement is required to achieve further reductions in deposition. In particular, the increased importance of regional transport results partly from the varied progress of emission controls between developed and developing regions. To reduce health risks from air pollution, stringent measures have commonly been implemented in densely populated urban areas, with many heavy industrial plants moved to nearby suburban towns or the countryside. Increased air pollution has been consequently detected in medium-sized towns that surround the JJJ, YRD and PRD megacities[22]. Effective emission controls for those areas should be the next important undertaking for both the improvement of regional air quality and the alleviation of deposition risk.

Uncertainties result from the estimations of both deposition and emissions. On the one hand, we developed GAM based on the observed bulk deposition, 30% of which has been reported as dry deposition, on average[23]. Dry deposition was found to contribute more to the total deposition in western and northern China than that in eastern and southern regions (Supplementary Table 5). Therefore, the reliance on bulk deposition as a metric undervalues

Table 2 | Relative contributions of nonlinear response of SNA to emissions and regional transport of pollution to the changes of SNA/*E*

Factors	Region	SNA/*E* for SO_4^{2-}		SNA/*E* for NO_3^-	
		Nonlinear formation (%)	Regional transport (%)	Nonlinear formation (%)	Regional transport (%)
Before 2010	JJJ	25	75	23	77
	YRD	43	57	41	59
	PRD	22	78	81	19
	SCB	13	87	54	46
After 2010	JJJ	49	51	66	34
	YRD	32	68	53	47
	PRD	37	63	57	43
	SCB	12	88	59	41

the role of dry deposition, particularly in less developed regions of China. In addition, the representativeness of individual observation sites may change over time. Influenced by increased human activities, such as industrial production and transportation, elevated deposition has been observed for some rural or suburban sites recently, but such impacts are limited at remote sites[24].

On the other hand, emissions estimation with bottom-up methods is substantially influenced by the researchers' understanding of emission processes and the selection of data, particularly for countries with insufficient emission monitoring and imperfect energy statistics[25]. For instance, FGD systems installed in China's power sector were not operated fully before 2010[26], and no information is currently available on the possible lax management of gypsum produced from FGD (for example, reuse in the cement industry), which could lead to a remobilization of the SO_2. Along with the increased penetration of emission control devices, supervision should be greatly improved to guarantee their full operation. As illustrated earlier, the improved operations of FGD and SCR are expected to reduce the uncertainties of emission and *D*/*E* estimation over the recent years (Supplementary Fig. 7). With enhanced controls on heavy industry, moreover, small-scale activities, such as residential burning of fossil fuels, which are not fully recorded in official statistics, may be responsible for a growing share of emissions. Manufacturing and combustion technologies, modes of energy consumption and fuel qualities are much more diverse than those for major industrial plants. An improved estimation of small-scale sources is thus greatly needed to further reduce the uncertainties of emission estimations and the evaluation of source–sink relationships.

Online content

Any methods, additional references, Nature Research reporting summaries, source data, extended data, supplementary information, acknowledgements, peer review information; details of author contributions and competing interests; and statements of data and code availability are available at https://doi.org/10.1038/s41561-022-00899-1.

Received: 9 April 2021; Accepted: 12 January 2022;
Published online: 21 February 2022

References

1. Zheng, B. et al. Trends in China's anthropogenic emissions since 2010 as the consequence of clean air actions. *Atmos. Chem. Phys.* **18**, 14095–14111 (2018).
2. Crippa, M. et al. Gridded emissions of air pollutants for the period 1970–2012 within EDGAR v4.3.2. *Earth Syst. Sci. Data* **10**, 1987–2013 (2018).
3. Stevens, C. J. et al. Impact of nitrogen deposition on the species richness of grasslands. *Science* **303**, 1876–1879 (2004).
4. Bowman, W. D. et al. Negative impact of nitrogen deposition on soil buffering capacity. *Nat. Geosci.* **1**, 767–770 (2008).
5. Liu, X. J. et al. Enhanced nitrogen deposition over China. *Nature* **494**, 459–462 (2013).
6. Yu, G. R. et al. Stabilization of atmospheric nitrogen deposition in China over the past decade. *Nat. Geosci.* **12**, 424–429 (2019).
7. Xia, Y. M., Zhao, Y. & Nielsen, C. P. Benefits of China's efforts in gaseous pollutant control indicated by the bottom-up emissions and satellite observations 2000–2014. *Atmos. Environ.* **136**, 43–53 (2016).
8. Krotkov, N. A. et al. Aura OMI observations of regional SO_2 and NO_2 pollution changes from 2005 to 2015. *Atmos. Chem. Phys.* **16**, 4605–4629 (2016).
9. Flower, D. et al. Nonlinearities in source receptor relationships for sulfur and nitrogen compounds. *Ambio* **34**, 41–46 (2005).
10. Zhang, X. Y. et al. Decadal trends in wet sulfur deposition in China estimated from OMI SO_2 columns. *J. Geophys. Res. Atmos.* **123**, 10796–10811 (2018).
11. Wesely, M. L. & Hicks, B. B. A review of the current status of knowledge on dry deposition. *Atmos. Environ.* **34**, 2261–2282 (2000).
12. Wen, Z. et al. Changes of nitrogen deposition in China from 1980 to 2018. *Environ. Int.* **144**, 106022 (2020).
13. Zhou, K. et al. Declining dry deposition of NO_2 and SO_2 with diverse spatiotemporal patterns in China from 2013 to 2018. *Atmos. Environ.* **262**, 118655 (2021).
14. Liu, M. et al. Rapid SO_2 emission reductions significantly increase tropospheric ammonia concentrations over the North China Plain. *Atmos. Chem. Phys.* **18**, 17933–17943 (2018).
15. Li, H. Y. et al. Rapid transition in winter aerosol composition in Beijing from 2014 to 2017: response to clean air actions. *Atmos. Chem. Phys.* **19**, 11485–11499 (2019).
16. Wang, G. H. et al. Persistent sulfate formation from London fog to Chinese haze. *Proc. Natl Acad. Sci. USA* **113**, 13630–13635 (2016).
17. Xing, J. et al. Nonlinear response of ozone to precursor emission changes in China: a modeling study using response surface methodology. *Atmos. Chem. Phys.* **11**, 5027–5044 (2011).
18. Li, M. et al. Persistent growth of anthropogenic non-methane volatile organic compound (NMVOC) emissions in China during 1990–2017: drivers, speciation and ozone formation potential. *Atmos. Chem. Phys.* **19**, 8897–8913 (2019).
19. Jin, X. & Holloway, T. Spatial and temporal variability of ozone sensitivity over China observed from the Ozone Monitoring Instrument. *J. Geophys. Res. Atmos.* **120**, 7229–7246 (2015).
20. Wang, S. X. et al. Impact assessment of ammonia emissions on inorganic aerosols in East China using response surface modeling technique. *Environ. Sci. Technol.* **21**, 9293–9300 (2011).
21. Yu, T. et al. Long-term trends in acid neutralizing capacity under increasing acidic deposition: a special example of eutrophic Taihu Lake, China. *Environ. Sci. Technol.* **50**, 12660–12668 (2016).
22. Zhang, Q. et al. Satellite remote sensing of changes in NO_x emissions over China during 1996-2010. *Chin. Sci. Bull.* **57**, 2857–2864 (2012).
23. Xu, W. et al. Quantifying atmospheric nitrogen deposition through a nationwide monitoring network across China. *Atmos. Chem. Phys.* **15**, 12345–12360 (2015).
24. Xu, W. et al. A database of atmospheric nitrogen concentration and deposition from the nationwide monitoring network in China. *Sci. Data* **6**, 51 (2019).
25. Zhao, Y., Zhang, J. & Nielsen, P. The effects of recent control policies on trends in emissions of anthropogenic atmospheric pollutants and CO_2 in China. *Atmos. Chem. Phys.* **13**, 487–508 (2013).
26. Xu, Y. Improvements in the operation of SO_2 scrubbers in China's coal power plants. *Environ. Sci. Technol.* **45**, 380–385 (2011).

Methods

Estimation of anthropogenic emissions. The MEIC was developed with a bottom-up methodology, in which the information relevant to emission estimations is collected and compiled from energy and economy statistics, industry investigations, regular air pollution source census and monitoring, and available field measurements, by region and source category. The inventory included five main source categories, that is, power plant, industry, residential, transportation and agriculture. The emissions were calculated as a product of the activity data and corresponding condition-specific emission factors (emissions per unit activity level):

$$\mathrm{EMI} = \sum_{s}\sum_{p}\sum_{m}(A_{s,p,m} \times \mathrm{EF}_{s,p,m}) \quad (1)$$

where EMI is the total emissions, s, p and m represent the source type, province and month, respectively, A is the activity data of a specific condition and EF is the corresponding emission factor. The emissions are allocated at a horizontal resolution of 0.25°×0.25°, according to the locations of power and industrial plants, population and economic densities, land cover, road network and other proxies. Details of the methods are presented in Zheng et al.[1].

Besides MEIC, we collected other available Chinese emission inventories within the research period for comparison. Those include the Emissions Database for Global Atmospheric Research[2], Regional Emission Inventory in Asia[27,28], the inventory for evaluating the climate and air quality impacts of short-lived pollutants[29] and the NH_3 emission inventory developed by Peking University[30].

Another approach to develop emission inventories is inverse modelling, or the so called top-down methodology. It applies satellite observation data to constrain the emissions by reducing the discrepancy between the observed and simulated VCDs and taking observation and model errors into account. Although uncertainty exists as well, the method is considered to be more independent of the energy and economy statistics. In this work, we collected a series of SO_2 and NO_x emission estimates based on the top-down methodology to evaluate the diversity of emission data and D/E ratio[31–39].

Estimation of bulk deposition and dry deposition. We applied a nonlinear GAM to estimate the monthly bulk deposition all over China at a horizontal resolution of 0.25°×0.25°, and then aggregated them into the annual totals. The model takes both linear and nonlinear correlations between the response variable (bulk deposition in the training dataset in this study, as described below in Ground-level observation of bulk deposition) and selected predictor variables (meteorological factors and satellite-derived VCDs, and so on, described later in this section) into consideration, and includes the interactive effects of precipitation and VCDs. Without the strict linearity assumption, the likelihood (or a quasi-likelihood) of bulk deposition is a sum of smooth functions of predictor variable[40]:

$$g(\mu_m) = \sum_{i=1}^{n} f_i(x_{i,m}) + \sum_{r,q} f_{rq}(x_{r,m}, x_{q,m}) + X_m\theta + \varepsilon_m \quad (2)$$

where g is the 'link' function, which specifies the relationship between the response variable μ and the linear formulation on the right side of the equation, $f_i(x_i)$ is the nonlinear smooth function that explores the single effect of individual predictor variable x_i (i is the index of variable for which a single effect was considered), n represents the total number of predictor variables for which a single effect was considered in the model, $f_{rq}(x_r,x_q)$ is a nonlinear smooth function that explores the interaction effect of predictor variables x_r and x_q (r and q are the indexes of variables for which an interaction effect was considered), $X\theta$ represents an ordinary linear model component for the predictors (elements of the vector $\mathbf{X}$) not subject to nonlinear transformations and ε represents the residuals of the models.

The smooth functions $f_i(x_i)$ and $f_{rq}(x_r,x_q)$ were fitted by thin-plate regression splines and tensor product smoothing, respectively. The interaction effects between precipitation and SO_2, NH_3 and/or NO_2 VCDs were considered in this work. As suggested in Zhang et al.[10], precipitation and VCDs were treated as interactive predictors, as abundant bulk deposition occurs with high levels of precipitation and atmospheric concentrations. Additionally, we used the restricted maximum likelihood method to choose appropriate knots to decide the degree of function smoothness, because the restricted maximum likelihood smoothing parameter selection tends to avoid occasional severe undersmoothing and is expected to provide the best simulations[41]. With an assumption of normal distribution, Gaussian distribution and the log link function were applied for the model residuals.

Supplementary Table 6 summarizes all the candidate variables, and multiple regressions were then applied to select the strong predictor variables for GAM construction. By adding variables in sequence to the model, the changed coefficient of determination (R^2) and Akaike information criterion were applied to evaluate the contribution of the variables to the model improvement, and the relatively stable R^2 and Akaike information criterion imply that the important predictor variables were already included in the model. Supplementary Fig. 14 provides an example for SO_4^{2-} and, in this case, predictor variables 9–11 (boundary layer height, relative humidity and total column ozone) were identified as less important to the model of SO_4^{2-} deposition prediction compared with that of other variables. After eliminating the redundant variables, the predictor variables in the full GAM were finally determined according to the results of a statistical significance test. For all the three species, the predictor variables contained precipitation, satellite-derived VCD, $PM_{2.5}$ (particles with aerodynamic diameter smaller than 2.5 μm) concentration, total column liquid water, temperature, boundary layer height, forest cover and urban cover. The hypothesis test results shown in Supplementary Table 7 indicate that the constructed GAMs include six predictor variables with P values smaller than 0.001 for each species.

We assessed the model assumptions and performance. We illustrate the frequency histograms of the model residuals to check their distribution in Supplementary Fig. 15. The model residuals have close to normal distribution, which suggests that the error of model fitting is random and that the selection of predictor variables is reasonable. The model concurvity (the fact that a smooth term in GAM could be approximated by one or more of the other smooth terms) is assessed by three indices—'Worst', 'Observed' and 'Estimate'—calculated with the Mixed GAM Computation Vehicle (MGCV) package in the R language. The indices judge the similarity of the smooth term for a given predictor variable with those of the others. All the indices were bound between 0 and 1, with 0 indicating no problem and 1 indicating a total lack of identifiability. In general, Worst is a fairly pessimistic measure, as it looks at the worst case irrespective of data, whereas Observed could be overoptimistic in some cases. Estimate is expected to be the most suitable for concurvity evaluation. As summarized in Supplementary Table 8, Estimate ranges between 0.1 and 0.5 for most cases, which indicates a limited concurvity for GAM. The potential overfitting of the model is examined with a tenfold cross validation. Comparing Supplementary Fig. 16a–f, the R^2 values of GAM decrease moderately with the cross-validation, which indicates a small overfitting of the model. Supplementary Figure 16g–i compares the predicted bulk deposition with GAM based on the training datasets and the observed ones in the evaluation datasets (described below in Ground-level observation of bulk deposition). The R^2 values were calculated at 0.6, 0.5 and 0.6, and the root mean squared prediction errors were 1.3, 0.7 and 0.6 for SO_4^{2-}, NO_3^- and NH_4^+, respectively. Despite a small overestimation of NO_3^- deposition, the models proved good capabilities of bulk deposition prediction.

We applied two datasets of dry deposition to explore its different responses to emissions compared with those of bulk deposition. Owing to a lack of direct measurement, the dry deposition of both datasets was estimated with an inferential method, that is, the deposition flux was calculated as the product of surface concentration and the dry deposition velocity (V_d) for a given species. In particular, one dataset includes the dry deposition of OXN and RDN at individual sites of the Chinese Nationwide Nitrogen Deposition Monitoring Network (NNDMN) from 2011 to 2018[12], and another includes the gridded dry deposition of SO_2 and NO_2 at a horizontal of 0.25°×0.25° across China from 2013 to 2018[13]. The surface concentration was measured for the former, whereas a random forest algorithm was applied to obtain the spatial pattern of concentration for the latter, based on the hourly observation data at 1,400 sites across the country (China National Environmental Monitoring Center, http://data.epmap.org/pollutions). The V_d for both datasets was simulated with a global chemistry transport model, GEOS-Chem (https://geos-chem.seas.harvard.edu/).

Analysis of factors that contribute to the variation of bulk deposition. The relative contribution of a given predictor variable to the variation of bulk deposition is judged according to the fraction to the total variability in the bulk deposition explained by the predictor. As the predictors might be correlated, we applied dominance analysis that considers the direct effect of each predictor and its joint effect with other predictors when partitioning the predictable criterion variance among them[42]. Certain single-predictor variables or multiple ones in the full GAM were picked and fitted into the GAM to develop a series of submodels. The overall R^2 of a given predictor variable was then computed based on all the possible submodels relevant to the predictor. The average increment in R^2 associated with a predictor across all the possible submodels is a quantitative measure of the predictor importance[43]. The conditional dominance of a predictor variable for each submodel was evaluated and the predictor variable with the highest average conditional dominance was identified as the largest contributor.

Analysis of factors that influence the response of bulk deposition to emissions. To evaluate the effect of the aerosol formation chemistry and regional transport of pollution on the D/E ratio, we simulated the SNA concentration with an air quality RSM, as a substantial uncertainty exists in the simulation of deposition by current air quality models[44,45]. RSM is a reduced-form prediction model that uses statistical correlation structures to approximate model functions through the design of complex multidimensional experiments[17,20]. It characterizes the relationship between model outputs and input parameters in a highly economical manner. The RSM model was developed by hundreds of simulations with the Community Multiscale Air Quality (CMAQ) modelling system, and the nonlinear responses of SNA concentrations to the precursor emissions (SO_2, NO_x, NH_3, VOCs and primary particles) were established. The meteorological fields were fixed at the 2017 level from the Weather Research and Forecasting model. The details of modelling setting are described in a previous study[46]. To justify the application of

SNA in the analysis, we examined the correlation between SNA and deposition from the CMAQ simulation, and that between the SNA from CMAQ and bulk deposition from GAM across the country. The correlation coefficients with SNA were larger than 0.7 and 0.8 for wet and total deposition, respectively, from the CMAQ simulation and larger than 0.7 for the bulk deposition from GAM for all the concerned three species (Supplementary Fig. 11).

Four scenarios were set in this study, Base, No-Local-Emis, No-Species-Chg and No-Region-Diff. In the Base scenario, we applied the MEIC emissions inventory as the emission input to represent the actual interannual spatiotemporal changes in China's air pollutant emissions from 2005 to 2020. In No-Local-Emis, the emissions in the concerned region of the four key regions (JJJ, YRD, PRD and SCB) were set as zero, and those in other areas in the country were set the same as in Base. The difference between Base and No-Local-Emis was regarded as the contribution of local emissions to the ambient SNA levels. In No-Species-Chg, the emissions of the concerned pollutant (SO_2, NO_x or NH_3) were the same as those in Base, whereas the emissions of other species for the whole research period were kept unchanged at the 2010 level. The differences between Base and No-Species-Chg thus reflect the effect of the nonlinear response of SNA to the changed emissions of multiple pollutants. In No-Region-Diff, the emissions in the concerned region (JJJ, YRD, PRD or SCB) are the same as those in Base, and the relative interannual changes in emissions for other areas in the country were assumed to be the same as those in the concerned region. The disparity of Base and No-Region-Diff reflect the effect of regional transport on SNA levels.

The RD between Base and No-Species-Chg or No-Region-Diff for species j (sulfur, OXN or RDN) and region k (JJJ, YRD, PRD or SCB) were calculated with equations (3) and (4):

$$\mathrm{RD}_{\mathrm{No-Species-Chg},j,k} = \left(\frac{\mathrm{CSNA}_{\mathrm{Base},j,k}}{E_{\mathrm{Base},j,k}} - \frac{\mathrm{CSNA}_{\mathrm{No-Species-Chg},j,k}}{E_{\mathrm{No-Species-Chg},j,k}}\right) \Big/ \left(\frac{\mathrm{CSNA}_{\mathrm{Base},j,k}}{E_{\mathrm{Base},j,k}}\right) \times 100\% \quad (3)$$

$$\mathrm{RD}_{\mathrm{No-Region-Diff},j,k} = \left(\frac{\mathrm{CSNA}_{\mathrm{Base},j,k}}{E_{\mathrm{Base},j,k}} - \frac{\mathrm{CSNA}_{\mathrm{No-Region-Diff},j,k}}{E_{\mathrm{No-Region-Diff},j,k}}\right) \Big/ \left(\frac{\mathrm{CSNA}_{\mathrm{Base},j,k}}{E_{\mathrm{Base},j,k}}\right) \times 100\% \quad (4)$$

where CSNA and E represent the simulated concentrations of SNA species and the emissions of the corresponding precursor in MEIC, respectively.

Ground-level observation of bulk deposition. The observation data of monthly ground-level bulk deposition were collected from NNDMN during 2010–2014, East Asia Acid Deposition Monitoring Network (EANET) during 2000–2015 and Chinese Ecosystem Research Network (CERN) from 2007–2010. As shown in Supplementary Fig. 1, the CERN sites are located in the North China Plain, and the EANET sites in four cities (Chongqing, Xi'an, Xiamen and Zhuhai). The NNDMN sites are located across the country. Supplementary Table 9 summarizes the basic information of the sites. There were a total of 61 sites involved in this analysis, and they are representative in geographical location and land use type. Of these, 64% are located in the relatively developed regions with a dense population and economy, which include northern (29%), central (12%), eastern (16%) and southern China (7%), with 36% in the less developed northeastern (7%), northwestern (13%) and southwestern China (16%). Of all the sites, 33, 46 and 21% are urban–industrial, rural–suburban–agricultural and background–remotes sites, respectively. In particular, rural–suburban and background–remote sites should be 20 and 50 km away from large pollution sources, respectively, and 500 m away from main roads. The three monitoring networks are well operated and maintained by the China Agricultural University, Asia Center for Air Pollution Research and Chinese Academy of Science, respectively. Uniform standard procedures for sampling, storage and chemical analysis were undertaken by trained personnel, with a full formal quality-control system. Quality assurance are routinely (commonly once every 20 samples) performed using standard samples during each analysis run. The differences between the determined and 'theoretical' results from the standard samples were controlled as less than ±5%.

Therefore, the best available observation data of bulk deposition were guaranteed to be applied in this work. The datasets were published as high-quality scientific databases[24]. More detailed information on the site selection, measurement protocol and quality assurance and/or quality control can be found in Xu et al.[23,24], Pan et al.[47,48] and the EANET monitoring manual[49]. For sulfur deposition, data from EANET were used to construct the model (that is, the training dataset) and those from CERN were used to evaluate the constructed model (that is, the evaluation dataset). For nitrogen deposition, data from NNDMN were used to construct the model, and data from EANET and CERN were merged to evaluate the models.

Satellite-derived VCDs. The tropospheric VCDs of NO_2 were derived from the Ozone Monitoring Instrument (OMI) on board the Aura satellite. In this study, the new version of the Peking University OMI level-2 NO_2 tropospheric product POMINO v2 dataset[50] from 2005 to 2020 was used (http://www.pku-atmos-acm.org/~acm/acmProduct.php/#POMINO). The algorithm is based on the AMFv6 package that calls the LIDORT v3.6 Radiative Transfer Model[50]. To be consistent with the ground-level deposition, the monthly NO_2 VCDs were calculated as the means of daily VCDs with the invalid values (when cloud coverage was >25%) excluded.

The planetary boundary layer VCDs of SO_2 were derived from the OMI as well. The OMI daily L3e (Level 3e) product[51] from 2005 to 2020 (https://disc.gsfc.nasa.gov/datasets/OMSO2e_V003/summary?keywords=Aura) was used for the calculation of the monthly mean VCDs. The product was retrieved using an algorithm based on principal component analysis, which presents considerable sensitivity for anthropogenic emissions[52]. The exclusion criteria contained 13 conditions, which included the observation time, local calendar dates before and/or after the L3e day, solar eclipse possibility flag set, row anomaly flag set, a radiative cloud fraction and the solar zenith angle (https://acdisc.gesdisc.eosdis.nasa.gov/data/Aura_OMI_Level3/OMSO2e.003/doc/README.OMSO2e.pdf).

The total VCDs of NH_3 were derived from the Infrared Atmospheric Sounding Interferometer on MetOp-A platform. The standard daily Infrared Atmospheric Sounding Interferometer/Metop-A ULB-LATMOS total column Level-2 product v2.2.0[53] was available from 2008 (https://iasi.aeris-data.fr/nh3_iasi_a_arch/). The method is based on the calculation of a spectral hyperspectral range index and subsequent conversion to the total NH_3 VCDs via a neural network. The daily column was excluded when the cloud coverage was >25%, the relative error was >100% or the absolute error was $>5\times10^{15}$ molecules cm^{-2}.

The Kriging method was applied to fill the missing values at the monthly average level, and the spatial pattern of the VCDs was obtained at a horizontal resolution of 0.25°×0.25°.

Other data. The monthly ground precipitation data from 2005 to 2020 at 824 sites across the country were obtained from the China Meteorological Administration (available at http://data.cma.cn/data/). The ordinary Kriging method was applied to map the data at the resolution of 0.25°×0.25°.

Other meteorological data were obtained from the European Centre for Medium-Range Weather Forecasts[54] at a 0.25°×0.25° resolution, which includes the temperature (K) at 2 m above the displacement height, relative humidity (%), total column liquid water (kg m^{-2}), boundary layer height (m), and wind speed at 10 m (m s^{-1}).

The monthly ground-level $PM_{2.5}$ concentration data at the 0.25°×0.25° resolution were obtained from Ma et al.[55] for 2005–2015. Based on the strong relationship between $PM_{2.5}$ and satellite-derived aerosol optical depth, Ma et al.[55] developed a geographically weighted regression model to estimate the $PM_{2.5}$ concentrations using the optical depth observations from the Moderate-Resolution Imaging Spectroradiometer. The spatial distributions of $PM_{2.5}$ concentrations for 2016–2020 were obtained with the Kriging interpolation method based on the hourly observation data at 1,400 sites across the country (China National Environmental Monitoring Center, https://data.epmap.org/page/index).

Land-use and land-cover change data were obtained from the Resource and Environment Data Cloud Platform (http://www.resdc.cn/), generated by manual visual interpretation of Landsat TM/ETM remote sensing images. We created a buffer zone (60 km in diameter) around each site of bulk deposition observation and calculate the area fractions of forest and town in the buffer zone to represent the degree of urbanization.

Data availability

Source data are provided with this paper.

Code availability

The code used to develop the GAM model for deposition estimation is available at https://figshare.com/s/975d70e28612f96e64b2.

References

27. Kurokawa, J. et al. Emissions of air pollutants and greenhouse gases over Asian regions during 2000–2008: Regional Emission inventory in ASia (REAS) version 2. *Atmos. Chem. Phys.* **13**, 11019–11058 (2013).
28. Kurokawa, J. & Ohara, T. Long-term historical trends in air pollutant emissions in Asia: Regional Emission inventory in ASia (REAS) version 3. *Atmos. Chem. Phys.* **20**, 12761–12793 (2020).
29. Klimont, Z. et al. Global anthropogenic emissions of particulate matter including black carbon. *Atmos. Chem. Phys.* **17**, 8681–8723 (2017).
30. Kang, Y. et al. High-resolution ammonia emissions inventories in China from 1980 to 2012. *Atmos. Chem. Phys.* **16**, 2043–2058 (2016).
31. Chen, Y. et al. Interannual variation of reactive nitrogen emissions and their impacts on $PM_{2.5}$ air pollution in China during 2005–2015. *Environ. Res. Lett.* **16**, 125004 (2021).
32. Ding, J. Y. et al. Intercomparison of NO_x emission inventories over East Asia. *Atmos. Chem. Phys.* **17**, 10125–10141 (2017).
33. Itahashi, S. et al. Inverse estimation of NO_x emissions over China and India 2005–2016: contrasting recent trends and future perspectives. *Environ. Res. Lett.* **14**, 124020 (2019).
34. Koukouli, M. E. et al. Updated SO_2 emission estimates over China using OMI/Aura observations. *Atmos. Meas. Tech.* **11**, 1817–1832 (2018).

35. Li, C. et al. India is overtaking China as the world's largest emitter of anthropogenic sulfur dioxide. *Sci. Rep.* **7**, 14304 (2017).
36. Miyazaki, K. et al. Decadal changes in global surface NO_x emissions from multi-constituent satellite data assimilation. *Atmos. Chem. Phys.* **17**, 807–837 (2017).
37. Qu, Z. et al. Monthly top-down NO_x emissions for China (2005–2012): a hybrid inversion method and trend analysis. *J. Geophys. Res. Atmos.* **122**, 4600–4625 (2017).
38. Qu, Z. et al. SO_2 emission estimates using OMI SO_2 retrievals for 2005–2017. *J. Geophys. Res. Atmos.* **124**, 8336–8359 (2019).
39. Qu, Z. et al. Hybrid mass balance/4D-Var joint inversion of NO_x and SO_2 emissions in East Asia. *J. Geophys. Res. Atmos.* **124**, 8203–8224 (2019).
40. Hastie, T. J. & Tibshirani, R. J. *Generalized Additive Models* (Chapman & Hall, 1990).
41. Simon, N. W. *Generalized Additive Models: An Introduction with R* 2nd edn (Chapman & Hall/CRC, 2006).
42. Johnson, J. W. A heuristic method for estimating the relative weight of predictor variables in multiple regression. *Multivariate Behav. Res.* **35**, 1–19 (2000).
43. Budescu, D. V. Dominance analysis: a new approach to the problem of relative importance of predictors in multiple regression. *Psychol. Bull.* **114**, 542–551 (1993).
44. Ge, B. Z. et al. Model inter-comparison study for Asia (MICS-Asia) phase III: multimodel comparison of reactive nitrogen deposition over China. *Atmos. Chem. Phys.* **20**, 10587–10610 (2020).
45. Itahashi, S. et al. MICS-Asia III: overview of model intercomparison and evaluation of acid deposition over Asia. *Atmos. Chem. Phys.* **20**, 2667–2693 (2020).
46. Xing, J. et al. Development and application of observable response indicators for design of an effective ozone and fine-particle pollution control strategy in China. *Atmos. Chem. Phys.* **19**, 13627–13646 (2019).
47. Pan, Y. P. et al. Identifying ammonia hotspots in China using a national observation network. *Environ. Sci. Technol.* **52**, 3926–3934 (2018).
48. Pan, Y. P. et al. Wet and dry deposition of atmospheric nitrogen at ten sites in northern China. *Atmos. Chem. Phys.* **12**, 6515–6535 (2012).
49. EANET *Data on the Acid Deposition in the East Asian Region* (Network Center for EANET, accessed 28 January 2022); https://monitoring.eanet.asia/document/public/index
50. Liu, M. Y. et al. Improved aerosol correction for OMI tropospheric NO_2 retrieval over East Asia: constraint from CALIOP aerosol vertical profile. *Atmos. Meas. Tech.* **12**, 1–21 (2019).
51. Krotkov, N. A. et al. *OMI/Aura Sulfur Dioxide (SO_2) Total Column L3 1 Day Best Pixel in 0.25° × 0.25° V3* (Goddard Earth Sciences Data and Information Services Center, 2015).
52. Li, C. et al. A fast and sensitive new satellite SO_2 retrieval algorithm based on principal component analysis: application to the ozone monitoring instrument. *Geophys. Res. Lett.* **40**, 6314–6318 (2013).
53. Damme, M. V. et al. Version 2 of the IASI NH_3 neural network retrieval algorithm: near-real-time and reanalysed datasets. *Atmos. Meas. Tech.* **10**, 4905–4914 (2017).
54. Johnson, S. J. et al. SEAS5: the new ECMWF seasonal forecast system. *Geosci. Model Dev.* **12**, 1087–1117 (2019).
55. Ma, Z. W. et al. Estimating ground-level $PM_{2.5}$ in China using satellite remote sensing. *Environ. Sci. Technol.* **48**, 7436–7444 (2014).

Acknowledgements

This work was sponsored by the National Key Research and Development Program of China (2017YFC0210106 to Y.Z., W.X., X.L. and Y.P.) and the Natural Science Foundation of China (41922052 to Y.Z. and 42177080 to Y.Z., M.M. and K.Z.).

Author contributions

Y.Z. designed the research. Y.Z., M.X. and Z.D. performed the research. Q.Z. and B.Z. processed the emissions data. W.X., Z.W., X.L. and Y.P. provided observational deposition data. M.M., K.Z., J.X., C.P.N., Y.L. and L.Z. interpreted the data. Y.Z., M.X. and C.P.N. wrote the paper with input from all the co-authors.

Competing interests

The authors declare no competing interests.

Additional information

Extended data is available for this paper at https://doi.org/10.1038/s41561-022-00899-1.

Supplementary information The online version contains supplementary material available at https://doi.org/10.1038/s41561-022-00899-1.

Correspondence and requests for materials should be addressed to Yu Zhao.

Peer review information *Nature Geoscience* thanks Stefan Reis and Thorjorn Larssen for their contribution to the peer review of this work. Primary Handling Editors: Simon Harold and Xujia Jiang, in collaboration with the *Nature Geoscience* team.

Reprints and permissions information is available at www.nature.com/reprints.

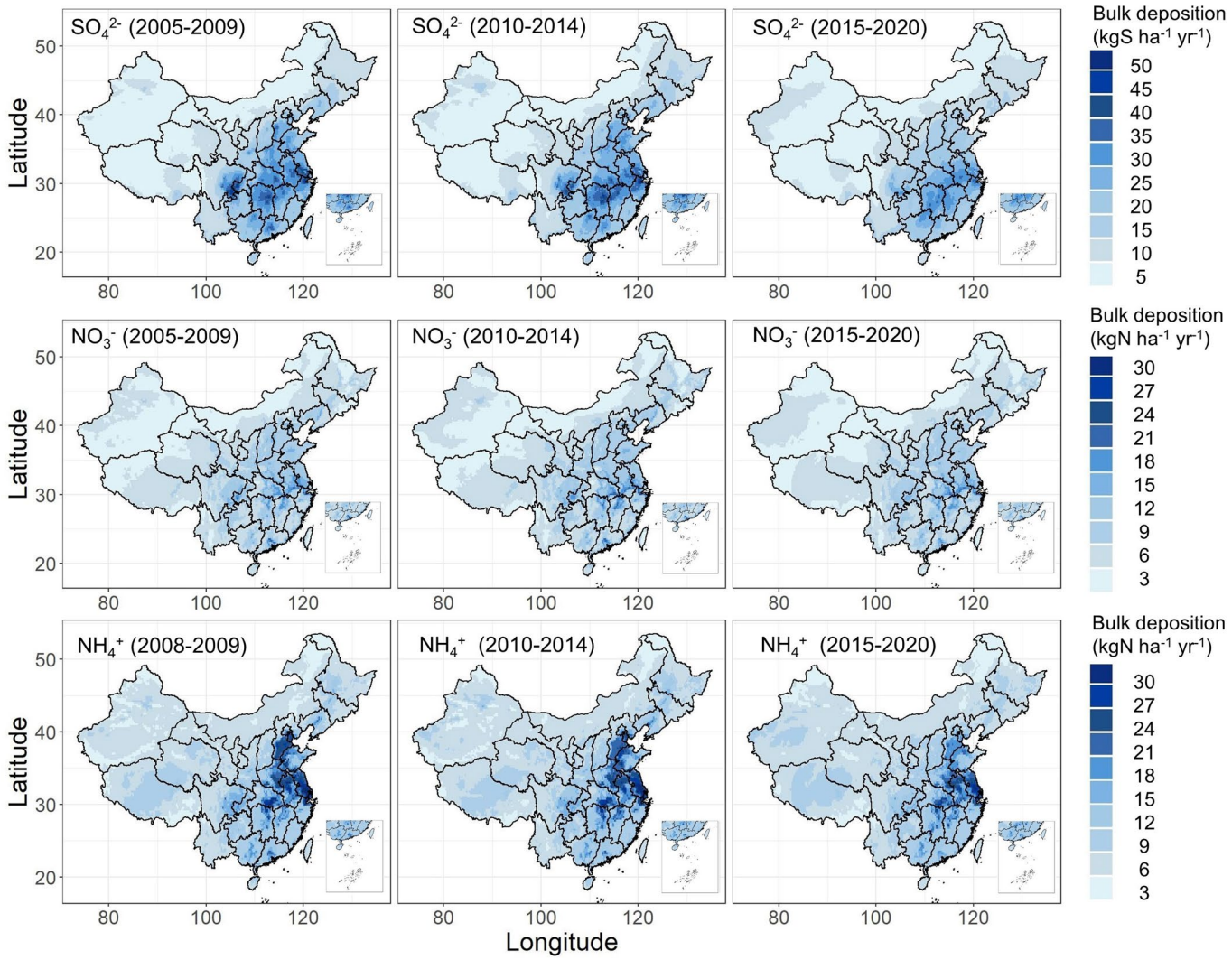

Extended Data Fig. 1 | The spatial patterns of average annual deposition of SO_4^{2-}, NO_3^-, and NH_4^+ over China. The left, central and right column indicate the average for 2005-2009 (2008-2009 for NH_4^+), 2010–2014, and 2015–2020, respectively. The horizontal resolution is 0.25°(lat)×0.25°(lon).

Extended Data Table 1 | The annual average bulk deposition of SO_4^{2-}, NO_3^- and NH_4^+ and the annual average emissions of anthropogenic SO_2, NO_X and NH_3 during 2005–2020 (2008-2020 for RDN) by region, and their fractions to the national total

Region	SO_4^{2-} deposition		NO_3^- deposition		NH_4^+ deposition	
	kgS $ha^{-1}·yr^{-1}$	Fraction %	kgN $ha^{-1}·yr^{-1}$	Fraction %	kgN $ha^{-1}·yr^{-1}$	Fraction %
JJJ	15.8	5.4	7.9	5.6	12.3	8.2
YRD	25.1	13.4	10.4	9.8	16.9	11.3
PRD	19.1	3.2	6.7	3.8	9.5	2.1
SCB	21.2	5.5	8.9	4.7	10.2	4.3
China	9.6	/	4.8	/	6.5	/

Region	SO_2 emissions		NO_X emissions		NH_3 emissions	
	kgS $ha^{-1}·yr^{-1}$	Fraction %	kgN $ha^{-1}·yr^{-1}$	Fraction %	kgN $ha^{-1}·yr^{-1}$	Fraction %
JJJ	57.1	15.8	57.1	15.6	26.8	11.7
YRD	30.1	11.2	44.5	16.2	23.3	11.2
PRD	19.7	2.8	26.9	4.4	15.1	2.9
SCB	38.1	8.4	18.7	4.7	29.8	8.4
China	11.2	/	10.7	/	8.4	/

The deposition data are obtained from GAM prediction in this work and the emissions are obtained from MEIC.